

## **Supplemental Material: Focused fluid flow structures potentially caused by solitary porosity waves:**

### **METHODS**

#### **Chimney Detection**

Chimney cubes abased on supervised self-educating neural networks were used to identify chimneys on seismic images (Connolly, 2015; Tingdahl et al., 2001). Vertical hydrocarbon migration is recognized in normally processed seismic data as zones of vertically aligned low reflectivity chaotic seismic signature due to the scatter of the seismic signal because of residual gas or fracturing. The procedure involved identifying obvious chimneys on key seismic lines and time or depth slices based on their tie to known or suspected direct hydrocarbon indicators. Non-chimneys are also picked in chaotic areas where vertical hydrocarbon migration is not supposed, such as debris flows or polygonal faulting. Seismic attributes (amplitude, energy, frequency, phase, dip, azimuth, similarity, and coherence measures) that distinguish between chimneys and non-chimneys are then calculated at the picked locations. The results are fed into a neural network for training. The results are then displayed on the key seismic lines to compare the neural network results with the interpreter's picks. When satisfied with the results, the neural network is applied to the entire 3D or 2D volume. The results are then validated via criteria, and valid chimneys can be displayed as 3D geobodies. Chimney cube is used together with structural, stratigraphic, and geophysical interpretations to understand the relation of identified chimneys to source rock, reservoir trap, or other geological bodies and structures.

#### **Chimney Modeling**

Essentially, pressure buildup leads to changes in the effective stresses in rock masses. Open fracture, shear fracture, or even more ductile processes of deformation localization might be initiated depending on the magnitude of shear stresses, rock mechanical properties, and the rate at which stress changes (Jaeger et al., 2007). Time-dependent viscous deformation significantly alters deformation localization processes. Very fast loading in the lab leads to instantaneous elastoplastic deformation and generation of fractures. However, most of the reservoir rocks quickly develop viscous deformation even without changes in applied stresses. Accumulation of viscous deformation in most reservoir rocks occurs on a timescale of a few hours (Makhnenko and Podladchikov, 2018). During slow loading experiments, samples have time to accumulate significant ductile dilation before generating any macroscopic fracture. On the other hand, viscous deformation in fluid saturated rocks is known to cause the spontaneous self-localization of porous fluid flow due to mechanical instability, called "solitary porosity waves" (Connolly and Podladchikov, 2007; Yarushina et al., 2020).

Solitary porosity waves were previously suggested as a mechanism of focused fluid flow in both magmatic and petroleum systems (Barcilon and Lovera, 1989; Connolly and Podladchikov, 2007; Mckenzie, 1984; Räss et al., 2019). However, verification of this

mechanism in real case studies remains limited (Joshi et al., 2012). Besides, previous models predicted the formation of porosity waves at fluid pressures exceeding lithostatic stress, which limited acceptance of the porosity wave mechanism. Our simulations are based on a new model of porous flow in deformable poro-viscoelastoplastic rocks (Yarushina and Podladchikov, 2015; Yarushina et al., 2020), which does not require unrealistically high fluid pressures. Fluid flow in porous rocks is controlled by the continuity equations for the fluid and the rock:

$$\frac{\partial(1-\varphi)}{\partial t} + \nabla_j \left( (1-\varphi) v_j^s \right) = 0 \quad (1)$$

$$\frac{\partial\varphi}{\partial t} + \nabla_j \left( \varphi v_j^f \right) = 0 \quad (2)$$

force balance equation in the rock:

$$\nabla_j \bar{\sigma}_{ij} - g \bar{\rho} \hat{z}_i = 0 \quad (3)$$

and Darcy's law for porous flow:

$$\varphi \left( v_i^f - v_i^s \right) = -\frac{k}{\mu} \left( \nabla_i p_f + g \rho_f \hat{z}_i \right) \quad (4)$$

where  $\varphi$  is porosity,  $t$  time,  $v^s, v^f$  the velocity of solid and fluid,  $\bar{\sigma}$  total stress tensor,  $g$  gravity,  $\mu$  fluid viscosity,  $p_f$  fluid pressure,  $\hat{z}$  upward-directed unit vector,  $\rho_f$  fluid density,  $\bar{\rho}$  the total density of the fluid and solid. For simplicity, fluid and solid rock grains are assumed to be incompressible and total compressibility of the fluid-saturated rock results from compaction of pore space.

Laboratory data for most reservoir rocks indicate that their instantaneous response is elastoplastic, while long-term behavior has a noticeable viscous component. Carbonates, shales, sandstones, and unconsolidated sands exhibit viscous creep in laboratory experiments (Brantut et al., 2013; Chang and Zoback, 2009; Croize et al., 2013; Hangx et al., 2010; Makhnenko and Podladchikov, 2018; Mondol et al., 2007; Nermoen et al., 2015). Other laboratory studies emphasize the dependence of rock permeability on effective pressure and porosity (Dong et al., 2010; van Noort and Yarushina, 2019). Our model builds on the recent experimental data and features stress-dependent permeability, stress, and porosity-dependent mechanical parameters. For permeability, we choose the expression:

$$k = k_0 \left( \varphi / \varphi_0 \right)^n \quad (5)$$

where  $k_0$  and  $\varphi_0$  are background values of the permeability and porosity, respectively; the exponent  $n$  is taken to be constant. Viscoelastoplastic stress-strain relations account for shear-induced dilation at positive effective pressures following experimental data (Yarushina et al., 2020):

$$\dot{\varepsilon} = \frac{\dot{\bar{p}} - \alpha \dot{p}_f}{K_d} + \frac{p_e - p_d}{\eta_{eff}} \quad (6)$$

$$\dot{\gamma}_{ij} = \frac{\dot{\tau}_{ij}}{2G_d} + \frac{\tau_{ij}}{2\eta_s} \quad (7)$$

where  $\dot{\varepsilon}$  is volumetric strain rate,  $\bar{p}$  is total pressure,  $p_e = \bar{p} - p_f$  is effective pressure,  $\tau_{ij}$  total stress deviator,  $\dot{\gamma}_{ij}$  is deviatoric strain rate,  $\alpha$  is Biot-Willis coefficient,  $K_d$  is the drained bulk modulus,  $G_d$  is the drained shear modulus, dot denotes material time derivative. Effective bulk and shear viscosities  $\eta_{eff}$  and  $\eta_s$  are taken in the form

$$\eta_{eff} = C \frac{\eta_0}{\varphi} \cdot \begin{cases} 1 & \text{if } F < 0 \\ \left[ (2\Lambda(F+1)\ln(F+1)+1)^{-1} \right] & \text{if } F \geq 0 \end{cases} \quad (8)$$

$$\eta_s = \eta_0 \begin{cases} 1 & \text{if } F < 0 \\ \left[ \Lambda \frac{3}{2\tau_0^2} (F+1) \ln(F+1) \left( 1 + \left( \frac{\tau}{\tau_0} \right)^2 \right)^{-1} + 1 \right]^{-1} & \text{if } F \geq 0 \end{cases} \quad (9)$$

In the plastic regime, they depend on the equivalent shear stress  $\tau^2 = \frac{3}{2} \tau_{ij} \tau_{ij}$  and effective pressure and reduce when stresses reach plastic failure limit:

$$F = \left( 1 + \left( \frac{\tau}{\tau_0} \right)^2 \right) \exp \left( \left( \frac{p_e - p_0}{Y} \right)^2 - 1 \right) - 1 \quad (10)$$

where  $p_0, Y, \tau_0$  are critical stresses that define failure envelope,  $\Lambda$  is dimensionless viscosity coefficient that shows how much viscosity changes with plasticity onset,  $\eta_0$  is the reference shear viscosity of the rock grains. The transition from dilation to compaction occurs at dilation pressure given as

$$p_d = \begin{cases} 0 & \text{if } F < 0 \\ 2\Lambda p_0 \frac{(F+1)\ln(F+1)}{2\Lambda(F+1)\ln(F+1)+1} & \text{if } F \geq 0 \end{cases} \quad (11)$$

Our model differs from most of the viscoplastic constitutive laws in that it allows viscous flow at stresses below the critical yield and allows dilation at positive effective pressures (Fig. S1). This constitutive model was implemented into high-resolution 2D numerical code using a Cuda-based pseudo-transient method (Omlin et al., 2018; Räss et al., 2019). This method allows the strong nonlinear coupling between flow and rock deformation to form localized fluid channels. As the spatial occurrence of focused fluid flow structures is not related to pre-existing fractures and thus not known in advance, we need high resolution in

the entire computational domain. This requires an efficient numerical strategy and the use of GPUs.

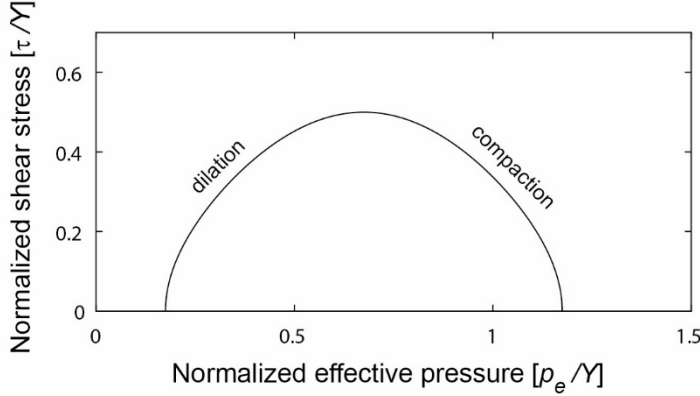


**Figure S1. Failure envelope defined by equation (10) corresponding to material parameters used for simulations.** The onset of plastic failure at pressures below 0.7 leads to the dilation of the pore space.

We nondimensionalize distances by the compaction length,  $L = \sqrt{\eta k / \mu}$ , time by the compaction time,  $T = \frac{\eta}{(\rho_s - \rho_f)gL}$ , and pressure by the characteristic compaction pressure,  $P = (\rho_s - \rho_f)gL$ . The characteristic scales reach  $L = 300$  m,  $T = 1$  yr and  $P = 2.9$  MPa for reference permeability  $k_0 = 7.2 \times 10^{-13}$ , fluid viscosity  $\mu = 8 \times 10^{-4}$  Pa · s, solid reference viscosity  $\eta_0 = 10^{14}$  Pa · s, density difference  $\rho_s - \rho_f = 10^3$  kg/m<sup>3</sup>, and  $g = 9.8$  m/s<sup>2</sup>. We keep the power-law index fixed at  $n = 3$ , and strength parameters in equations (8) - (11) at  $p_0 = 0.7$ ,  $\tau_0 = 0.8$ ,  $Y = 0.5$ ,  $\Lambda = 10$ ,  $C = 10$ . As an initial setup, we use a rectangular domain of stratified porous rock with dimensions of  $80L \times 10L$ . This corresponds to a vertical cross-section 24km wide and 3 km deep (Fig. 2). We incorporate each geological layer's depth and lithology data in our modeling to define the depths and thicknesses of the reservoir and other geological heterogeneities. Initial porosities of  $\phi_r = 0.35$  and  $\phi_0 = 0.075$  are assigned for the reservoir and background, respectively. A randomly distributed noise (30% of background porosity) is added everywhere in the computational domain to mimic the natural heterogeneous distribution of porosity. The numerical resolution is 2400x300 cells. The solid velocities  $v_x^s$  and  $v_y^s$ , are zeros, and the effective pressure,  $p_e$ , is constant at the boundaries. The only external force acting on the domain is gravity pointing downwards. Channels grow due to interplay between buoyancy that forces upward migration of fluid flow and viscoplastic rock deformation. Buoyancy creates a fluid pressure gradient. Slightly elevated fluid pressures at the upper part of the reservoir force dilation of the pore space, thus creating a space for upward fluid migration. Initial flow instability leads to disaggregation of the uniform fluid pressure front into separate fingers. These are further amplified by viscoplastic deformation of the porous rocks that tend to compact pore space in the areas with lower fluid pressure. Through time, separate channels are formed, propagating upward as a

self-sustained body (see Supplementary Movies). Fluid underpressure generated in the lower part of the channels leads to fluid diffusion from the background into the channels so that channels grow even further, and background porosity is reduced compared to initial values. The highly focused fluid pressure increase within the channel generates deviatoric stresses around the channel head, which further enhances rock deformation and pore dilation (Fig. 3). Due to shear stresses, dilation of pore space in viscoplastic rocks can be achieved at a relatively small increase of the fluid pressure, which might be way below the fracture limits.

Fluid leakage associated with chimney formation can be estimated from fluid flux through a given horizontal cross-section of the computational domain. It can be several orders of magnitude higher than the background fluid flux (Räss et al., 2019). This makes chimneys preferential fluid leakage pathways.

### **Role of Parameters and Model Limitations**

Our results apply to one-phase fluid flow, i.e., we ignore here capillary pressure and additional buoyancy effects that might arise in the presence of liquid and gas. Chimneys in our model are formed by increasing the fluid pressure due to the difference in density between the saturating fluid and host rock. The two-phase nature of the flow will only assist chimney formation as gas will be separated much faster. At the same time, capillary entry pressure will eventually be overcome by increasing fluid pressure.

Timescales of chimney propagation strongly depend on the characteristic compaction time,  $T$ . The distribution of chimneys is controlled by changes in reservoir topology, thickness, and the compaction length,  $L$ , defined above. In areas where the reservoir has significant changes in its thickness, chimney formation might be expected (Figs. 2 and 3). However, chimneys might develop even in homogeneous media from a reservoir with an utterly flat topology (e.g., Elenius et al., 2018, Fig. 13). In this case, their position and spacing will be determined by the compaction length.

In addition, the spacing between chimneys and their width where a reservoir has a flat upper surface or no thickness variation is determined by the physical properties of the rock and pore fluid, i.e., by the compaction length. In highly permeable and viscous rocks, one might expect wider channels to form, whereas channels will be narrow in tight rocks with low viscosity. Liquids will, in general, produce more narrow channels than gases. More viscous oils will create very narrow channels. In our models, the chimney needs only fractions (0.14) of the characteristic time to reach the seafloor. Liquids will, in general, produce more narrow chimneys than gases. Parameters assumed in our model correspond to liquid migration in sandstones. The characteristic scales for gas migration will be  $L = 1000\text{ m}$ ,  $T = 0.2\text{ yr}$  assuming gas viscosity  $\mu = 7 \cdot 10^{-5}\text{ Pa} \cdot \text{s}$  and density difference  $\rho_s - \rho_f = 1500\text{ kg/m}^3$ . In other words, gas chimneys will be three times wider than chimneys produced by liquid, and the time of their formation will be five times faster.

Natural permeability variations between different formations and rock types will also influence the size and spacing of chimneys. Reducing permeability by one order of magnitude will reduce the compaction length by factor 3 and increase the time of chimney formation by the same factor. In general, shales and clay-rich rocks are characterized by much lower permeability than sandstones. At the same time, their viscosity might be on the

$k = 10^{-18} \text{ m}^2$  and viscosity is

$\eta_0 = 10^{14} \text{ Pa} \cdot \text{s}$ , we obtain  $L = 1 \text{ m}$  and  $T = 180 \text{ yr}$  for gas flow and  $L = 0.3 \text{ m}$ ,  $T = 915 \text{ yr}$  for liquid flow. This implies that gas escaping the reservoir with thick shaley caprock might reach the seafloor in 25 years. The diameter of the expected crater will be on the order of a few meters and might be below the seismic resolution.

The timescale of chimney propagation also depends on permeability exponent  $n$ , which describes the degree of coupling between flow and deformation in the equation (5). Fig. S2a presents simulation results showing the dependence of chimney growth speed on the permeability exponent. As permeability exponent changes from  $n=2.5$  to  $n=4.5$ , the dimensionless time required to reach the seafloor ranges from 0.5 to 0.17. The larger the permeability exponent, the quicker the chimney develops. In general, shales are characterized by much higher permeability exponent  $n$  than sandstones (Dong et al., 2010). Thus, the time of chimney propagation in shales might be even faster than presented above.

The presence of various stratigraphic layers also influences chimneys. Time and length scales of chimney growth in each layer depend on the compaction length and compaction time for that layer. Simple dimensional analysis shows that reducing permeability by two orders of magnitude in a geological layer will reduce the speed of chimney growth in that layer by two orders of magnitude. Thus, in areas with tight rocks, chimney propagation will be significantly slower. Here, we investigate how uncertainty in permeability and bulk viscosity of the competent layer affects the results. We performed simulations where the permeability of the competent layer is reduced five times (Fig. S3a) or increased two times (Fig. S3b) in comparison to the model shown in Fig. 3. Results show that changes in permeability did not significantly affect the chimney propagation pattern and only influenced their growth rate. A twofold increase in permeability resulted in a slight reduction of arrival time compared to the original model shown in Fig. 3. Figs. S3a and S3b compare two different scenarios for the same period and show that the reservoir fluid is still contained by the seal at the end of simulations when permeability is reduced five times. Thus, sufficient permeability contrast will significantly delay upward fluid migration (Fig. S2b). However, the viscous nature of the rock and nonlinear coupling between flow and deformation will drive further chimney propagation.

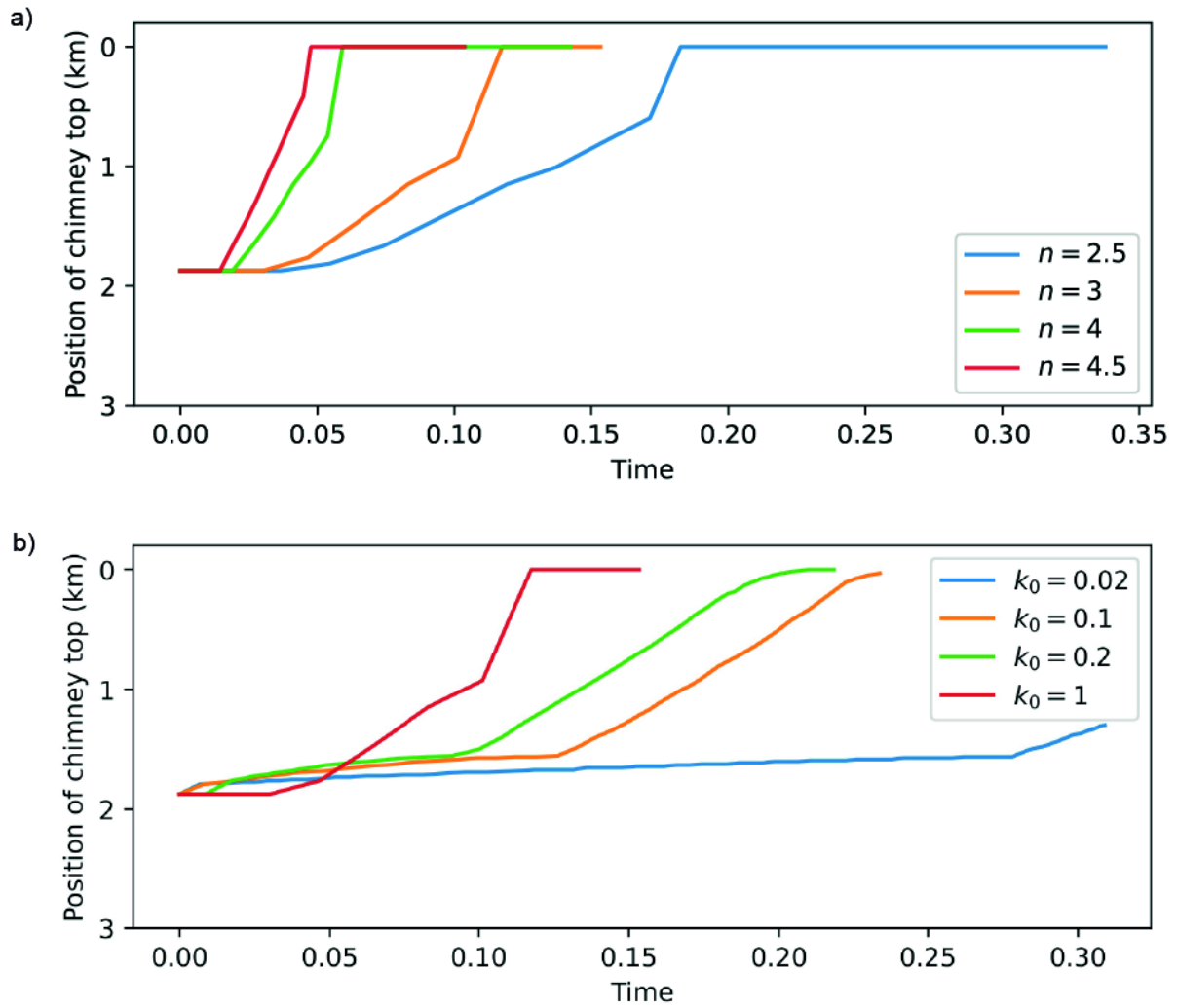


**Figure S2. The evolution of the position of the chimney top with time for different permeability parameters.** Time units are normalized to characteristic time,  $T$ . (a) Dependence of the chimney propagation time on different permeability exponents for the same background permeability  $k_0 = 1$ . (b) Dependence of the chimney propagation time on background permeability,  $k_0$ , for the same value of permeability exponent  $n = 3$ .

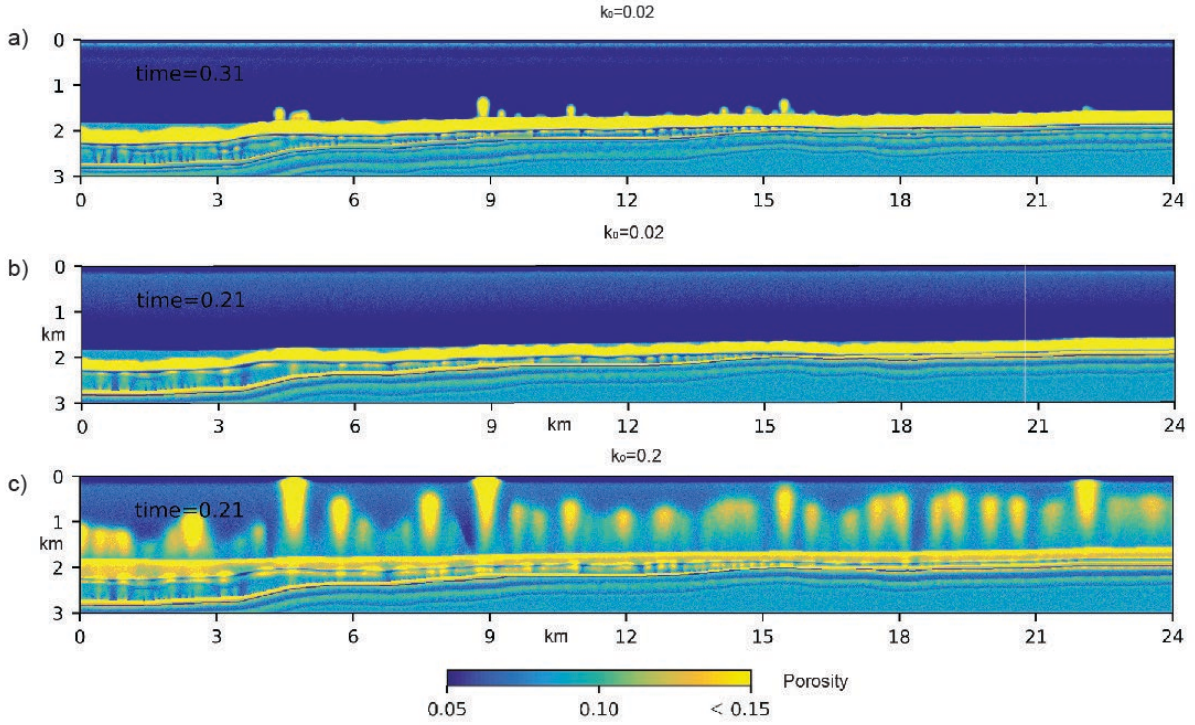


**Figure S3. Snapshots of chimney growth in a model with a competent layer**, in which permeability  $k_0$  is (a,b) fifty times smaller than background permeability  $k_b$  or (c) five times smaller than background permeability  $k_b$ .

Next, we vary the bulk viscosity of the competent layer. Fig. S4 compares the model without competent layer (Fig. S4a) with two different models where bulk viscosity is increased by a factor  $\Delta\eta = 9$  (Fig. S4b) or  $\Delta\eta = 36$  (Fig. S4c) in comparison to the background viscosity. A ninefold increase of viscosity leads to wider chimneys in the competent layer and the generation of a thin low-porosity layer at the top of the competent layer and a high-porosity layer at its bottom. Chimney growth is delayed in comparison with the case shown in Fig. S4a. The width of the chimney in the interval above the competent layer is also altered. Further increase of viscosity contrast to  $\Delta\eta = 36$  leads to further delay in chimney propagation. However, fluid still goes through the competent layer. The snapshot in Fig. S4c shows diffusive porosity distribution above the competent layer, and pronounced chimneys did not have time to form. However, given sufficient time chimneys will be developed, albeit broader, and with lower porosity contrast with the background porosity.

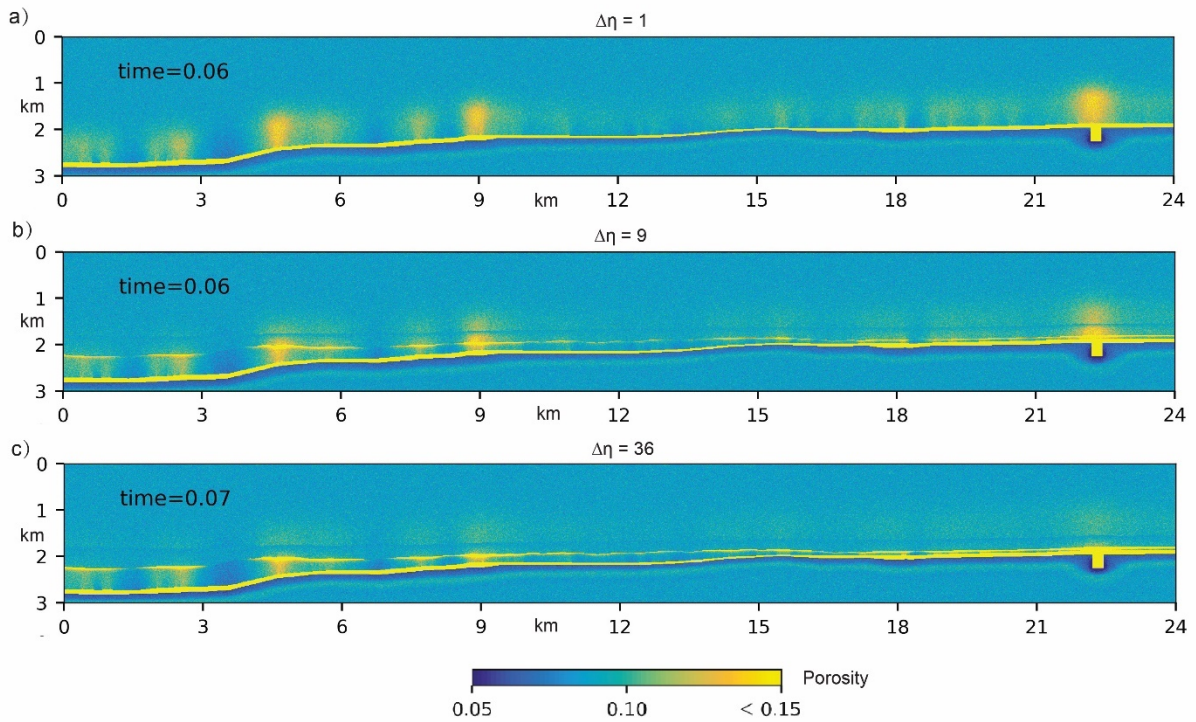


**Figure S4. Influence of a competent layer with higher viscosity on chimney growth.** (a) Snapshot for a model without a competent layer. (b) The competent layer has a viscosity that is nine times higher than the background value (c). The competent layer has a viscosity that is thirty-six times higher than the background value.

**Table S1. Technical specification of the survey**

Number of cables	12
Streamer length	6000 m
Number of channels	480
Channel interval	12.5 m
Streamer separation/depth	50 m/20 m
Inline offset	85 m
Shot interval	18.75 m
Source separation/depth	25 m/7 m
Source type	Sode. G guns II 2000 psi 4135 cu. in.
Instrument response	3.04Hz @7.5dB/Oct
Record length	7168 ms

## REFERENCES CITED

- Barcion, V., and Lovera, O. M., 1989, Solitary Waves in Magma Dynamics: *Journal of Fluid Mechanics*, v. 204, p. 121-133.
- Brantut, N., Heap, M. J., Meredith, P. G., and Baud, P., 2013, Time-dependent cracking and brittle creep in crustal rocks: A review: *Journal of Structural Geology*, v. 52, p. 17-43.
- Chang, C. D., and Zoback, M. D., 2009, Viscous creep in room-dried unconsolidated Gulf of Mexico shale (I): Experimental results: *Journal of Petroleum Science and Engineering*, v. 69, no. 3-4, p. 239-246.
- Connolly, D. L., 2015, Visualization of vertical hydrocarbon migration in seismic data: Case studies from the Dutch North Sea: *Interpretation-A Journal of Subsurface Characterization*, v. 3, no. 3, p. Sx21-Sx27.
- Connolly, J. A. D., and Podladchikov, Y. Y., 2007, Decompaction weakening and channeling instability in ductile porous media: Implications for asthenospheric melt segregation: *Journal of Geophysical Research-Solid Earth*, v. 112, no. B10, p. B10205.
- Croize, D., Renard, F., and Gratier, J. P., 2013, Compaction and Porosity Reduction in Carbonates: A Review of Observations, Theory, and Experiments: *Advances in Geophysics*, Vol 54, v. 54, p. 181-238.
- Dong, J. J., Hsu, J. Y., Wu, W. J., Shimamoto, T., Hung, J. H., Yeh, E. C., Wu, Y. H., and Sone, H., 2010, Stress-dependence of the permeability and porosity of sandstone and shale from TCDP Hole-A: *International Journal of Rock Mechanics and Mining Sciences*, v. 47, no. 7, p. 1141-1157.
- Elenius, M., Skurtveit, E., Yarushina, V., Baig, I., Sundal, A., Wangen, M., Landschulze, K., Kaufmann, R., Choi, J. C., Hellevang, H., Podladchikov, Y., Aavatsmark, I., and Gasda, S. E., 2018, Assessment of CO<sub>2</sub> storage capacity based on sparse data: Skade Formation: *International Journal of Greenhouse Gas Control*, v. 79, p. 252-271.
- Hangx, S. J. T., Spiers, C. J., and Peach, C. J., 2010, Creep of simulated reservoir sands and coupled chemical-mechanical effects of CO<sub>2</sub> injection: *Journal of Geophysical Research-Solid Earth*, v. 115.
- Jaeger, J. C., Cook, N. G. W., and Zimmerman, R. W., 2007, *Fundamentals of rock mechanics*, Malden, MA, Blackwell Pub., xi, 475 p. p.:
- Joshi, A., Appold, M. S., and Nunn, J. A., 2012, Evaluation of solitary waves as a mechanism for oil transport in poroelastic media: A case study of the South Eugene Island field, Gulf of Mexico basin: *Marine and Petroleum Geology*, v. 37, no. 1, p. 53-69.
- Makhnenko, R., and Podladchikov, Y. Y., 2018, Experimental Poroviscoelasticity of Common Sedimentary Rocks: *Journal of Geophysical Research-Solid Earth*, v. 123, no. 9, p. 7586-7603.
- Mckenzie, D., 1984, The generation and compaction of partially molten rock: *Journal of Petrology*, v. 25, no. 3, p. 713-765.
- Mondol, N. H., Bjorlykke, K., Jahren, J., and Hoeg, K., 2007, Experimental mechanical compaction of clay mineral aggregates - Changes in physical properties of mudstones during burial: *Marine and Petroleum Geology*, v. 24, no. 5, p. 289-311.
- Nerموen, A., Korsnes, R. I., Hiorth, A., and Madland, M. V., 2015, Porosity and permeability development in compacting chalks during flooding of nonequilibrium brines: Insights from long-term experiment: *Journal of Geophysical Research-Solid Earth*, v. 120, no. 5, p. 2935-2960.
- Omlin, S., Räss, L., and Podladchikov, Y. Y., 2018, Simulation of three-dimensional viscoelastic deformation coupled to porous fluid flow: *Tectonophysics*, v. 746, p. 695-701.

- Räss, L., Duretz, T., and Podladchikov, Y. Y., 2019, Resolving hydromechanical coupling in two and three dimensions: spontaneous channelling of porous fluids owing to decompaction weakening: *Geophysical Journal International*, v. 218, no. 3, p. 1591-1616.
- Tingdahl, K. M., Bril, A. H., and de Groot, P. F., 2001, Improving seismic chimney detection using directional attributes: *Journal of Petroleum Science and Engineering*, v. 29, no. 3-4, p. 205-211.
- van Noort, R., and Yarushina, V., 2019, Water, CO<sub>2</sub> and Argon Permeabilities of Intact and Fractured Shale Cores Under Stress: *Rock Mechanics and Rock Engineering*, v. 52, no. 2, p. 299-319.
- Yarushina, V. M., and Podladchikov, Y. Y., 2015, (De)compaction of porous viscoelastoplastic media: Model formulation: *Journal of Geophysical Research Solid Earth*, v. 120.
- Yarushina, V. M., Podladchikov, Y. Y., and Wang, H., 2020, Model for (de)compaction and porosity waves in porous rocks under shear stresses: *Journal of Geophysical Research: Solid Earth*, v. 125, p. e2020JB019683.